

Beating oscillations of magneto-optical spectra in simple hexagonal graphite

Rong-Bin Chen^a, Yu-Huang Chiu^{b,c,*}, Ming-Fa Lin^{b,*}

^aCenter of General Studies, National Kaohsiung Marine University, Kaohsiung 811, Taiwan

^bDepartment of Physics, National Cheng Kung University, Tainan 701, Taiwan

^cDepartment of Applied Physics, National Pingtung University, Pingtung 900, Taiwan

July 3, 2021

Abstract

The magneto-optical properties of simple hexagonal graphite exhibit rich beating oscillations, which are dominated by the field strength and photon energy. The former has a strong effect on the intensity, the energy range of the beating and the number of groups, and the latter modulates the total group numbers of the oscillation structures. The single-particle and collective excitations are simultaneously presented in the magnetorefectance spectra and can be precisely distinguished. For the loss function and reflectance, the beating pattern of the first group displays stronger intensities and broader energy range than other groups. Simple hexagonal graphite possesses unique magneto-optical characteristics that can serve to identify other bulk graphites.

Keywords: graphite; Landau subbands; magnetic field; dielectric function; collective excitations; beating patterns

* Corresponding author. Tel: +886-6-2159492.

E-mail addresses: airegg.py90g@nctu.edu.tw (Y.H. Chiu), mflin@mail.ncku.edu.tw (M.F. Lin)

1. Introduction

Graphene-based materials have attracted many researchers to investigate their physical properties due to their potential for novel applications. The material properties demonstrate their strong dependence on the stacking configurations [1–6], layer numbers [7–12], and interlayer atomic interactions [13–15]. Graphite is composed of van der Waals coupled graphene layers [16,17]. Three prototypes of periodical stacking along the z -direction exist: AA-stacked simple hexagonal graphite (SHG), AB-stacked Bernal graphite (BG), and ABC-stacked rhombohedral graphite (RHG). The graphites discovered in nature are mainly composed of BG and RHG. Recently, SHG has been successfully synthesized in the laboratory [18]. The interlayer couplings play an important role in determining the low-energy electronic properties; thus, different periodic stacking configurations exhibit their own unique characteristics. It is known that the neighboring electronic states congregate and form the Landau subbands (LSs) along \hat{k}_z in a perpendicular uniform magnetic field $\mathbf{B}=B_0\hat{z}$. The magneto-electronic properties demonstrate very interesting phenomena, e.g., the anisotropy of low-energy electronic structures [16,19–21], the de Haas-van Alphen effect [22,23], quantum Hall effect [24–27]. In this work, we mainly focus on obtaining the magneto-optical properties of SHG by means of evaluating the dielectric function $\varepsilon(\omega, B_0)$. Comparisons with BG and RHG are also made.

The LSs of graphites present many important features. SHG possesses very strong k_z -dependent energy dispersions with a broad band width about 1 eV, and each LS can be described by a simple relationship with k_z [19,25]. Many LSs cross the Fermi level ($E_F = 0$) [19,28]. Moreover, the excitations related to the densely low-lying LSs own wide energy ranges which can overlap for different optical transition channels. On the contrary,

RHG exhibits weak k_z -dependent dispersions with a narrow band width (~ 10 meV) [21]. Only one LS crosses E_F , and there is no coexisting energies for different optical excitations. The LS can be characterized by the approximate solution [29]. The energy dispersion of BG has a band width of ~ 0.2 eV, which lies between that of SHG and RHG, and two LSs cross E_F [30, 31]. The low-lying LSs are complex and cannot be easily described by k_z . The characteristics of LSs would be reflected in the magneto-optical spectra.

The magneto-optical properties are closely associated with the stacking configurations of graphites [28, 31–33]. The low-energy magneto-optical absorption spectrum of SHG is dominated by intraband and interband optical excitations which induce a multi-channel threshold peak, several two-channel peaks, and many double-peak structures [28]. In the magneto-optical absorption spectra of BG, the prominent peaks originate from the interband excitations at both the K and H points. The peaks associated with the K point display double-peak structures [20, 30]. Moreover, the field evolution of the absorption lines for the K -point type shows an approximately linear dependence, while the dependence of the H point is square-root like [20, 30, 34]. The magnetorefectance $R(\omega, B_0)$ spectra of BG displays irregular oscillations [35, 36]. Up to now, no theoretical calculations and experimental measurements for the magneto-optical absorption or reflection of RHG have been performed .

The magneto-optical properties are evaluated based on the Peierls tight-binding model, which can be exactly diagonalized even with the inclusions of field-induced Peierls phases and important atomic interactions in the Hamiltonian [28, 31, 37]. This study shows that the beating patterns of the dielectric function can be formed mainly owing to the strong overlap of different optical transition channels in a wide frequency range. Such beating patterns are

also exhibited in the higher-frequency absorption spectrum, loss function, and reflectance. The single-particle and collective excitations can be precisely identified, respectively, based on the shoulders (peaks) and dips of specific structures in the magnetorefectance spectra. The regular beating magneto-optical spectra can be controlled by the field strength and the photon energy, which provide a theoretical basis for future experiments to clarify the optical responses of the graphite configurations.

The generalized tight-binding model deserves a closer examination in numerical calculations. We developed this model to study the magneto-electronic and -optical properties by the exact diagonalization method. In studying the magneto-electronic properties, the earlier work can only cope with eigenvalues and eigenfunctions at strong magnetic field strength [38] because the Hamiltonian matrix gets too large as the field strength decreases. For example, this matrix is 40000×40000 for monolayer graphene at 7.9 T. By means of rearranging the tight-binding functions, it is possible to transform the huge matrix into a band-like one. Therefore, the eigenvalues and the wave functions can be efficiently solved at weaker field strength ($\sim 1\text{T}$) [37]. In this work, the magneto-optical absorption spectra, which are determined by three large matrices due to the Hamiltonian, the initial state and the final state, can be obtained by using the localized features of the magnetic wave functions. The PC clusters are sufficient in calculating numerical data. The acquired features of LS spectra and the reliable characterization of the LS wave functions provide a guideline for other physical properties, such as Coulomb excitations and transport properties. As for the discussion of the optical properties in our previously published works, the generalized tight-binding method has been successfully applied to investigate the magneto-optical absorption spectra of few-layer graphenes. The optical selection rules are well defined through

the detailed analysis on the wave functions. It is also applicable to bulk graphite with layers stacked in any sequence. Furthermore, the generalized tight-binding model can be used in the cases of spatially modulated fields and combined magnetic and electric fields.

2. Methods

For calculation purposes, the geometric structure of simple hexagonal graphite is regarded as a stacking sequence of infinite layers of graphene with an AA-stacked configuration along \hat{z} . All honeycomb structures in SHG have the same projections on the x-y plane. The interlayer distance is $I_c = 3.50 \text{ \AA}$ [18] and the C-C bond length is $b' = 1.42 \text{ \AA}$. A primitive unit cell consists of two atoms. The associated hopping integrals γ_i 's taken into account are the one intralayer atomic interaction ($\gamma_0 = 2.519 \text{ eV}$) and three interlayer atomic interactions ($\gamma_1 = 0.361 \text{ eV}$; $\gamma_2 = 0.013 \text{ eV}$; $\gamma_3 = -0.032 \text{ eV}$) [15].

When SHG is subjected to a $B_0\hat{z}$, the path integral of the vector potential induces a periodical Peierls phase (details in Ref. [19]). The phase term of the associated period is inversely proportional to the magnetic flux ($\Phi = 3\sqrt{3}b'^2B_0/2$) through a hexagon. To satisfy the integrity of the primitive cell, the ratio $R_B = \Phi_0/\Phi$ ($\Phi_0 = hc/e$ flux quantum) has to be a positive integer. As a result, the extended rectangular unit cell has $4R_B$ carbon atoms. The π -electronic Hamiltonian built from the $4R_B$ tight-binding functions is a $4R_B \times 4R_B$ Hermitian matrix. To solve this huge matrix problem, one can convert the Hamiltonian matrix into a band-like form by rearranging the tight-binding functions [19, 29, 31]. Both eigenvalue $E^{c,v}$ and eigenfunction $\Psi^{c,v}$ are efficiently obtained, even for a small magnetic field. The superscripts c and v , respectively, represent the conduction and valence bands.

The main features of the electronic properties can be directly manifested by optical

excitations. As materials absorb photons, electrons are excited from occupied states to unoccupied states. Within the relaxation-time approximation [39], the transverse dielectric function at zero temperature is expressed as

$$\begin{aligned} \varepsilon(\omega, B_0) = & \epsilon_0 - \frac{e^2}{\pi^2} \sum_{n,n'} \sum_{h,h'=c,v} \int_{1st\ BZ} d^3\mathbf{k} \frac{\left| \left\langle \Psi_{n'}^{h'}(\mathbf{k}) \left| \frac{\hat{\mathbf{E}} \cdot \mathbf{P}}{m_e} \right| \Psi_n^h(\mathbf{k}) \right\rangle \right|^2}{\omega_{hh'}^2(n, n'; \mathbf{k})} \\ & \times \left\{ \frac{1}{\omega - \omega_{hh'}(n, n'; \mathbf{k}) + i\Gamma} - \frac{1}{\omega + \omega_{hh'}(n, n'; \mathbf{k}) + i\Gamma} \right\}, \end{aligned} \quad (1)$$

where $\epsilon_0 = 2.4$ is the background dielectric constant [40]. $\omega_{hh'}(n, n'; \mathbf{k}) = E^{h'}(n', \mathbf{k}) - E^h(n, \mathbf{k})$ is the optical excitation energy which comes from the intraband ($c \rightarrow c; v \rightarrow v$) or interband excitations ($v \rightarrow c$); $\Gamma (= 3.5 \text{ meV})$ is the broadening parameter due to the deexcitation mechanisms. In these optical excitations, the momentum of the photons is nearly zero and thus the excitations can be regarded as a vertical transition between two LSs. The initial and final states have the same wavevector, i.e., $\Delta k_x = 0$, $\Delta k_y = 0$, and $\Delta k_z = 0$ [28]. The velocity matrix element $D_m = \left\langle \Psi_{n'}^{h'}(\mathbf{k}) \left| \frac{\hat{\mathbf{E}} \cdot \mathbf{P}}{m_e} \right| \Psi_n^h(\mathbf{k}) \right\rangle$ is evaluated within the gradient approximation [39, 41]. As $|D_m|^2 / \omega_{hh'}^2$ is set to be a constant, the imaginary part of $\varepsilon(\omega, B_0)$ is simply the joint density of states $D_J(\omega, B_0)$. The evaluation of $\varepsilon(\omega, B_0)$ can be employed to study the absorption spectrum, loss function, and reflectance.

3. Results and discussion

The perpendicular magnetic field causes the cyclotron motion in the x - y plane; therefore, the Landau levels lie on the k_x - k_y plane and the LSs along \hat{k}_z . The energy dispersions of the LSs along the $K - H$ line ($0 \leq k_z(\pi/I_c) \leq 1$) exhibit a strong dependence on k_z , as shown in Fig. 1. Based on the node structure of the Landau wave functions, the quantum number $n^c(n^v)$ for each conduction (valence) LS can be identified by the total number of

nodes [28]. The LSs with n^c and those with n^v are asymmetric about $E_F = 0$ because of the interlayer atomic interactions. In optical excitations, electrons are excited from occupied LSs into unoccupied LSs. For the sake of convenience, the excitations between two LSs with quantum numbers $n^{c,v}$ and $m^{c,v}$ are represented as $[n^{c(v)}, m^{c(v)}]$ and (n^v, m^c) for intraband and interband excitations, respectively. Moreover, the wave functions of occupied and unoccupied states offer important insights into the possible excitation channels. Since the LS wave functions of SHG are similar to those of monolayer graphene, the same selection rule $|\Delta n| = |m^{c,v} - n^{c,v}| = 1$ applies [28, 42, 43].

To investigate the spectrum structure of SHG, an illustration of optical excitations is exhibited in Fig. 1 to show the existence of intraband and interband optical excitations. The two intraband excitations $[n^c, (n+1)^c]$ and $[(n+1)^v, n^v]$ exhibit a tiny frequency discrepancy, and similar results are also obtained for the two interband excitations $(n^v, (n+1)^c)$ and $((n+1)^v, n^c)$. The former two and latter two can be simplified as $[n, n+1]$ and $(n, n+1)$, respectively. The intersection point of each LS with the Fermi level is the Fermi-momentum state, $k_F^{n^{c,v}}$. The effective k_z -range is confined by the initial and the final Fermi-momentum states, i.e., $k_F^{n^{c,v}} \leq k_z \leq k_F^{(n\pm 1)^{c,v}}$, as shown in Fig. 1 by the colored arrows. The intraband excitations with smaller $n^{c(v)}$'s possess a broader effective k_z -range (Fig. 1(a)). This reflects the fact that a quick decline of the energy spacing between two adjacent LSs due to increasing the quantum number $n^{c(v)}$'s. The effective k_z -ranges related to the interband excitations are larger than those of the intraband excitations; furthermore, they gradually grow in the increment of $n^{c(v)}$. This leads to an increase in the range of interband excitation frequency or the peak width in $D_J(\omega, B_0)$. This means that the effective k_z -ranges gradually grow as the frequency increases (Fig. 1(b)–(d)), and so

do the ranges of the interband excitation energies.

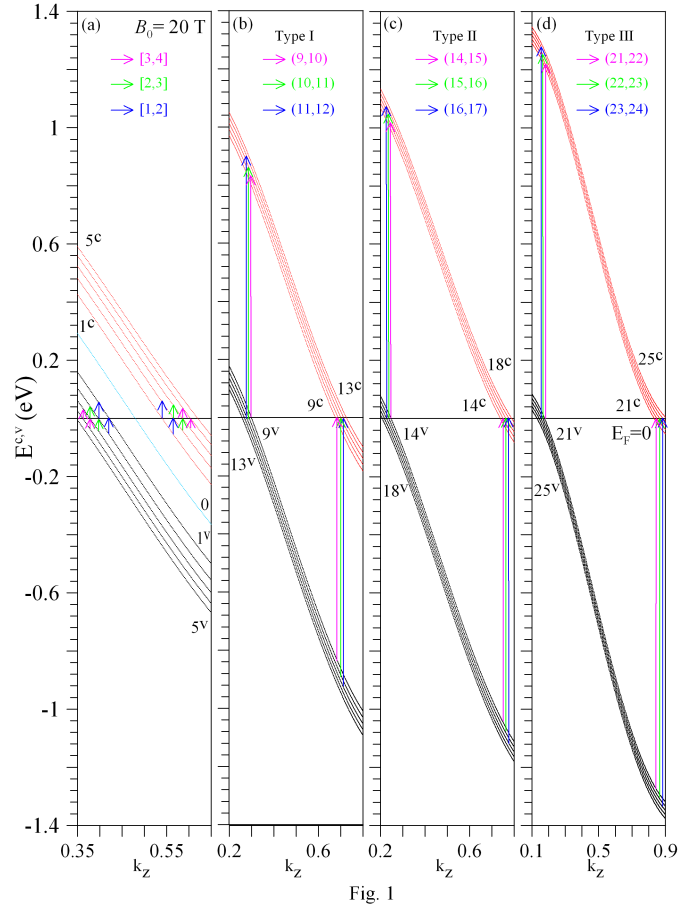


Figure 1: The vertical optical excitations at $B_0 = 20$ T due to the Landau subbands for (a) the intraband and (b)-(d) interband excitations. The allowed excitations are confined by two arrows of the same color. The square brackets and the parentheses represent the intraband and interband excitations, respectively.

The joint density of states is the number of optical excitation channels, which are directly reflected in the absorption spectra. The spectral function can be expressed by the imaginary part of $\varepsilon(\omega, B_0)$, i.e., $A(\omega) = \omega^2 \varepsilon_2 / 2\pi$. Each $D_J(\omega, B_0)$ peak originates from excitations within a certain k_z -range surrounded by the two arrows in Fig. 1. In each diagram, different colors are used to denote excitation channels corresponding to their own D_J peaks in Fig.

2. For the range $\omega < 0.1$ eV, the three higher-frequency D_J peaks of the intraband excitations, i.e., [1,2], [2,3], and [3,4], are indicated by blue, green, and magenta curves, respectively (Fig. 2(a)). These peaks partially overlap each other and such an overlap might cause that the peaks merge together in the optical spectrum, especially for the weak magnetic field cases. Moreover, each peak is a composite structure of two intraband excitation channels: $[n^c, (n+1)^c]$ and $[(n+1)^v, n^v]$. The peak strength grows with an increasing frequency because of the enlarged effective k_z -range.

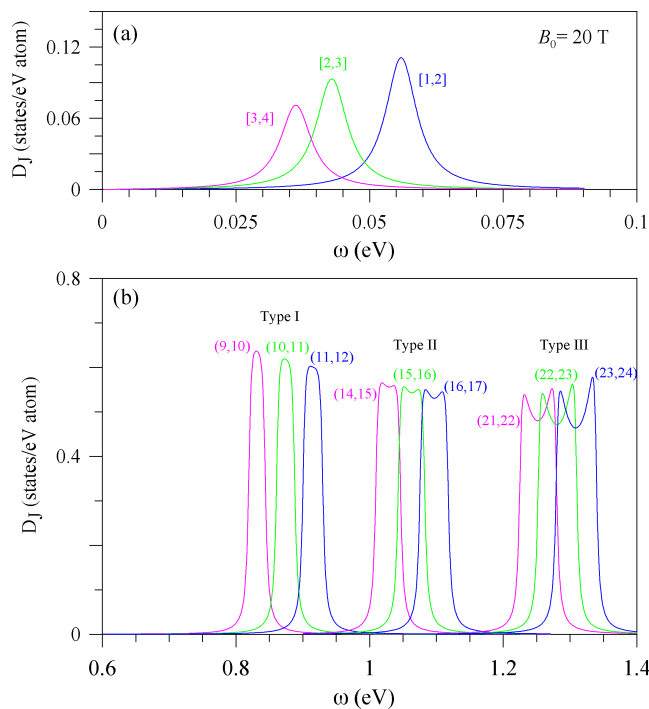


Fig. 2

Figure 2: The joint density of states corresponding to the Figure 1 for the (a) intraband (b) interband optical excitations.

In the frequency range $\omega \geq 0.1$ eV, the D_J peaks are related to the interband excitations as shown in Fig. 2(b). In the D_J , the three-peak structures associated with each type exhibit

different characteristics. This is a result of the fact that the k_z -dependent curvature variations between two LSs in a certain k_z region are discrepant. The former three peaks associated with the peaks of absorption spectrum $A(\omega)$, are distinguishable. These Type I peaks are located within the range $0.1 \text{ eV} < \omega < 1 \text{ eV}$ for a field strength of $B_0 = 20 \text{ T}$ (indicated by the red curve in Fig. 3(a)). Type II peaks are a combination of two neighboring peaks, such as (14,15) and (15,16) or (15,16) and (16,17). Their composite peak intensity is twice that of the original peaks. The peaks correspond to the absorption spectrum with higher-intensity peaks in the frequency range of $1 \text{ eV} < \omega < 1.25 \text{ eV}$ (Fig. 3(a)). As to Type III, three neighboring peaks are merged to a single peak and its intensity is enhanced to almost three times the original one. The D_J peaks show up in the spectral frequency range of $1.25 \text{ eV} < \omega < 1.45 \text{ eV}$. The higher-intensity absorption peaks are caused by the merging of yet more D_J peaks as a result of multiple channel excitations. This clearly indicates that absorption peak height is increased with the frequency following the sequence specified by the ω -range.

In the absence of a magnetic field, the optical absorption spectrum is indicated by the green curve in Fig. 3(a) and only a shoulder structure exists at $\omega \approx 1.5 \text{ eV}$ [41]. The magneto-optical spectrum demonstrates an abundance of absorption peaks. It is dominated by the intraband and interband excitations. The former lead to a stronger threshold peak and some weaker peaks ($\omega < 0.1 \text{ eV}$ for $B_0 = 20 \text{ T}$), while the many groups with a similar beating structure are attributed to the latter. The beating oscillations are mainly determined by the joint density of states, since the velocity matrix element is almost independent of the wave vector ($D_m \simeq 3\gamma_0 b'/2$). The width of the absorption peak gradually grows as the frequency increases. This leads to a higher degree of overlap for the neighboring two peaks, thus the Group I beating oscillations are formed within the range of $0.1 \text{ eV} < \omega < 1 \text{ eV}$. The frequency range associated with the other groups shifts to a higher frequency following their group numbers. The oscillation is weaker towards the end of each beating pattern. Moreover, these patterns are reflected in the dielectric function. $A(\omega)$ exhibits a

red shift in the spectrum, more groups and weaker intensity as the field strength decreases. The main reason is that the LS spacing, effective k_z -range of the LS and the state degeneracy are lowered with a decreasing B_0 .

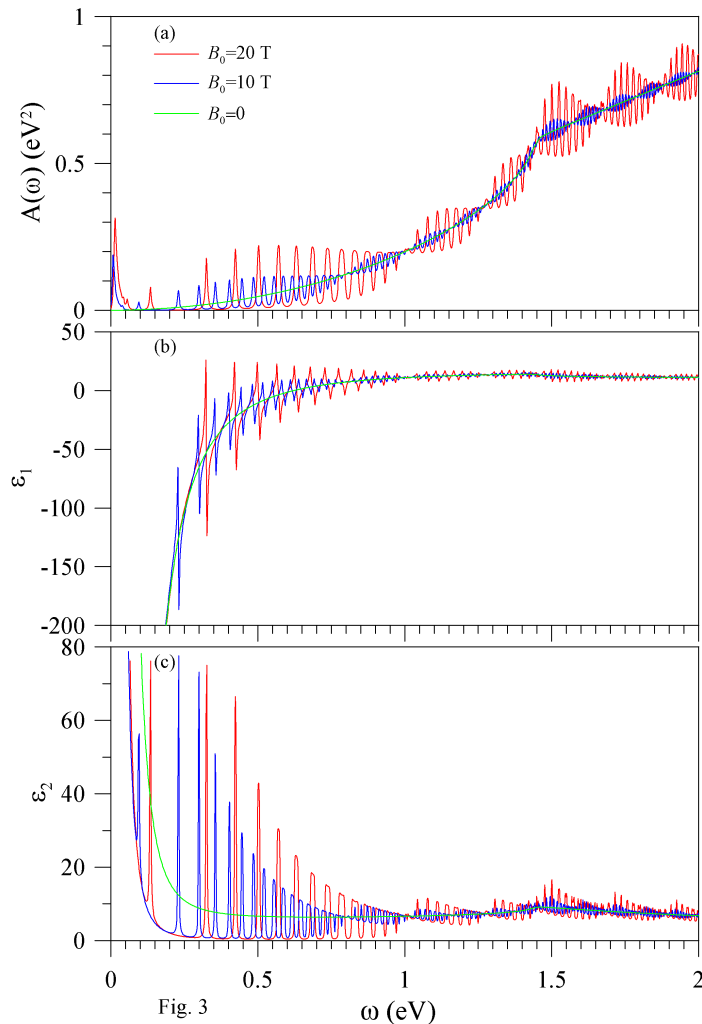


Figure 3: (a) The optical absorption spectrum, (b) the real part, and (c) the imaginary part of the dielectric function are shown for field strengths 20 T, 10 T and zero.

The single-particle excitations and collective plasmon modes can be characterized by the real part ϵ_1 and the imaginary part ϵ_2 of the dielectric function. Each allowed LS excitation produces a pair of asymmetric peaks in ϵ_1 and a peak in ϵ_2 , as shown in Fig. 3(b) and (c), respectively. If the zero points in ϵ_1 occur where ϵ_2 vanishes, they are associated with the undamped plasmon

oscillations. The peak strength presents a beating pattern in the dielectric function. Moreover, the magnitude of $\varepsilon(\omega, B_0)$ should diminish at higher frequencies, owing to the ω^{-2} factor in Eq. (1). It should also be noted that ε_1 and ε_2 , due to the intraband excitations, are quite large, e.g., their values are more than 10^3 times higher for $\omega < 0.05$ eV (not shown). Thus, they hardly contribute to the loss function and reflectance spectra, and do not induce prominent structures in such spectra. Moreover, the temperature only has an effect on the composite threshold peak which is caused by the intraband excitations [28]. As a result, the temperature effects are negligible in this work.

The loss function, defined as $Im[-1/\varepsilon(\omega, B_0)]$, is useful for understanding the collective excitations that can be measured by inelastic light and electron scattering spectroscopy [44–46]. The loss function presents many noticeable peaks, as shown in Fig. 4(a). These peaks are regarded as the collective excitations, only coming from the interband excitations. The peak structures belonging to Group I in terms of the energy range are prominent, whereas the other groups belonging to different types own weak plasmon peaks. The higher intensity corresponds to a zero point in ε_1 and a small value in ε_2 within the gap region between two single-particle excitation energies, while the lower intensity is subjected to strong Landau damping with a large ε_2 . The plasmon peaks first rise, and then decline with increasing LS transition channels. These peaks are gradually red-shifted and diminished with respect to the decrease of field strength.

The field-dependent plasmon frequency deserves a closer investigation in order to understand the LS features. The frequency of each plasmon structure grows with increasing field strength, as shown in Fig. 4(b). Plasmon peaks hardly survive in the loss function for a sufficiently weak field strength. The low critical field occurs at higher LS transition channels associated with a higher plasmon energy, while the lower LS transition channels are subjected to the high critical field. It is relatively easy to observe the plasmon peak for larger B_0 and ω . Due to the state degeneracy and effective k_z -range of LS being proportional to B_0 , the low field strength only presents a few

of plasmon peaks from the higher LS transition channels. As for $B_0 = 0$, one prominent plasmon peak arises at $\omega_p = 0.63$ eV (Fig. 4(a)).

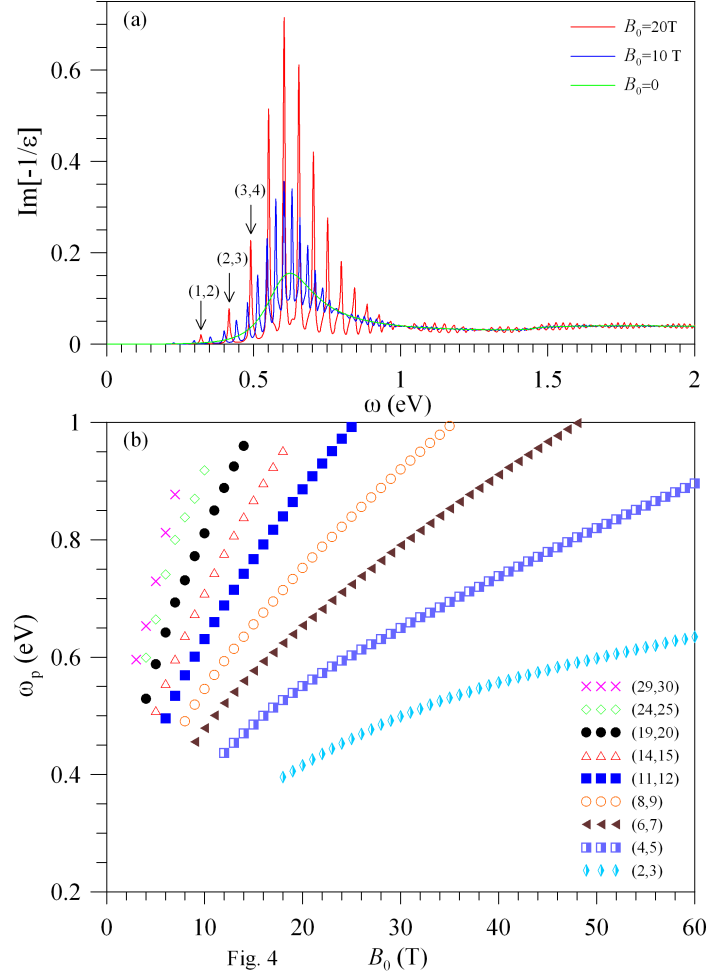


Figure 4: (a) The loss function with respect to three different field strengths. (b) Plasmon frequencies versus field strengths. Each curve corresponds to a specific interband excitation.

The magnetorefectance calculated from the $R(\omega, B_0) = \left|1 - \sqrt{\epsilon(\omega, B_0)}\right|^2 / \left|1 + \sqrt{\epsilon(\omega, B_0)}\right|^2$ clearly depicts the features of single-particle and collective excitations. The magnetorefectance spectrum presents a series of field-dependent oscillations in the beating pattern, compared with the featureless $R(\omega, B_0)$ at $B_0 = 0$ (Fig. 5(a)). The strongest beating pattern is located in the Group I. The magnetorefectance spectrum contains both shoulders (peaks) and dips, respectively,

indicating the single-particle and collective excitations. When the electromagnetic wave propagates in SHG, it is attenuated very rapidly for strong single-particle excitations with a very large ε_2 , and most of the electromagnetic power is reflected. On the other hand, if the electromagnetic wave frequency is the same as or higher than ω_p , the electromagnetic power is effectively absorbed by the collective excitations, resulting in the plasmon dip structures of the spectrum. The beating pattern diminishes its intensity and exhibits a red shift as the field strength decreases.

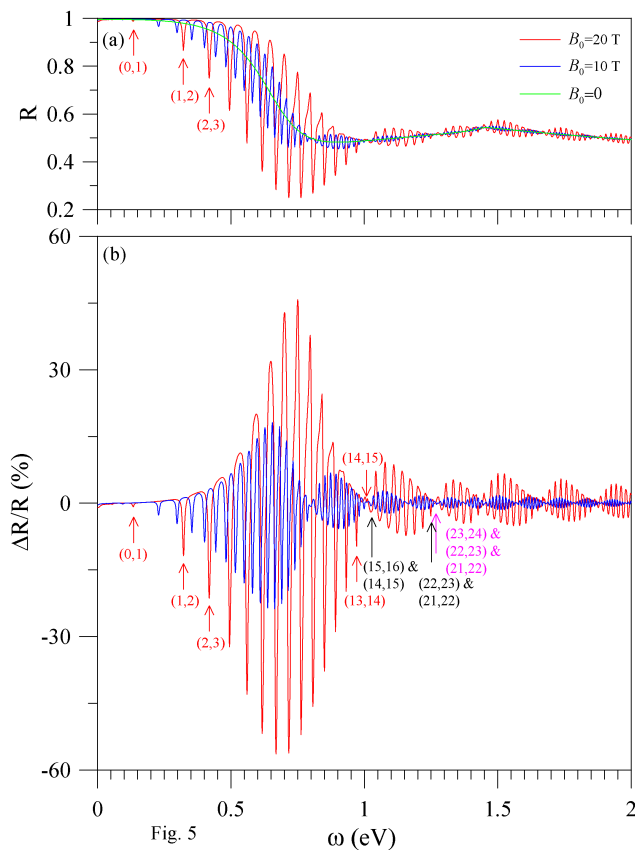


Figure 5: (a) The magnetorefectance spectrum and (b) the relative magnetorefectance spectrum for different field strengths.

The relative magnetorefectance, $\Delta R/R = (R(\omega, B_0) - R(\omega, 0))/R(\omega, 0)$ exhibits rather strong oscillations in the beating pattern for different frequency ranges, as shown in Fig. 5(b). The

beating patterns of Group I present stronger intensities and broader energy range than those of other groups. The strongest $\Delta R/R$ of the beating pattern of Group I is close to $\pm 50\%$ for $B_0 = 20$ T, but below $\pm 10\%$ for the other groups. These results could all be verified by experimental measurements. As the field strength decreases, the energy range of each beat pattern is decreased. It should be noted that up to now, the estimated variation ranges of $\Delta R/R$ are all less than 20% for other systems at the same field strength 20 T, e.g., Bernal graphite [35,36,47] and $\text{YBa}_2\text{Cu}_3\text{O}_y$ [48]. SHG is predicted to exhibit the largest variations in its magnetorefectance spectrum among all condensed-matter systems.

The $\Delta R/R$ with respect to the field strength reveals different groups of oscillation structures which could be tuned by the photon energies (Fig. 6). The shoulders (peaks) and dips are attributed to interband excitations. The oscillations still appear in the comparatively weak field associated with the higher LS transition channels. These results indicate that the oscillations move more rapidly to higher B_0 as the photon energy increases. In the range of $\omega < 0.5$ eV, all oscillations belong to Group I (Fig. 6(a)). The Group I and Group II oscillations coexist within the range of $0.5 \text{ eV} < \omega < 0.65 \text{ eV}$ (Fig. 6(b)). Thus, when photon energy increases, $\Delta R/R$ exhibits more groups, as shown in Fig. 6(c). Evidently, there exists a relationship between the critical photon energies and the group numbers, as these energies are identified to be 0.5 eV, 0.65 eV, 0.85 eV, etc.. This phenomenon is a unique characteristic of SHG and can be used to distinguish it from other graphene-related systems.

The oscillation structures of SHG are very different from those of the other graphites. SHG presents a few groups of oscillation structures with very strong $\Delta R/R$. The photon energy can be used to modulate the total number of groups as a result of the strong k_z -dependent LS dispersion and the wide overlapping ranges of energy for different transition channels. On the contrary, only low-energy irregular oscillation structures was found in BG [35,36,47,48]. The low-lying LS dispersions with a narrow energy width of ~ 0.2 eV are responsible for the absence of beating

oscillations. Up to now, no theoretical calculations or experiments on the oscillation structures of RHG have been performed. Based on the very weak LS dispersions and the lack of overlapping energy ranges of the different transition channels, RHG supposedly will only exhibit irregular oscillations of low intensities that will not demonstrate a beating pattern.

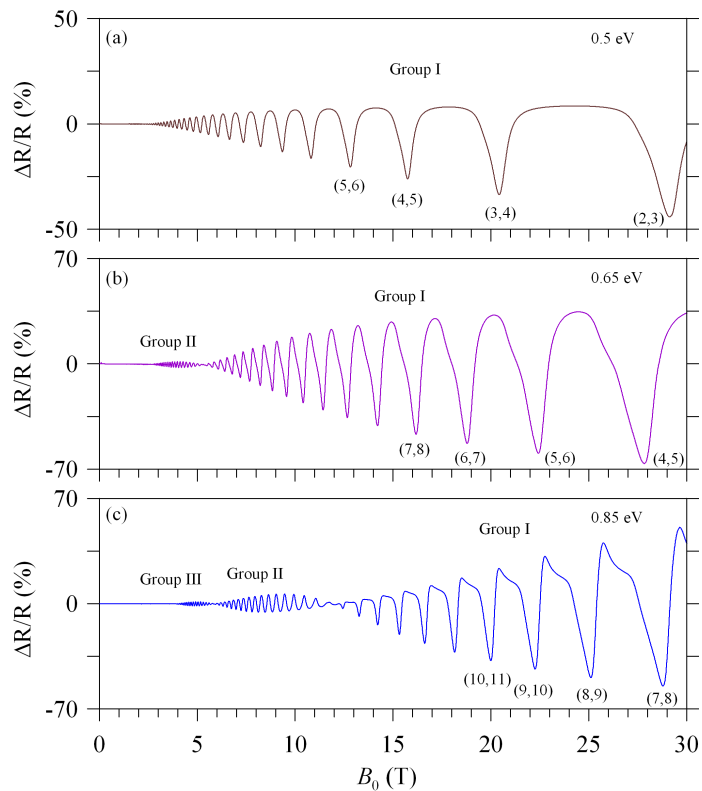


Fig. 6

Figure 6: The relative magnetorelectance with respect to the field strength reveals distinct groups of oscillation structures. Panels (a)-(c) represent different photon energies.

4. Conclusion

The magneto-optical properties of SHG demonstrate rich spectra with beating structures,

owing to the strong k_z -dependent LS and the wide overlapping ranges of energy for different transition channels. The single-particle excitations and collective excitations appear simultaneously in the magneto-optical spectra and can be precisely identified. The beating pattern of both the loss function and reflectance in Group I exhibit stronger intensities and wider energy ranges than those in other groups. As field strength increases, the plasmon peaks of the loss function and the dips of the reflectance are intensified, but the number of groups of beating structures is diminished. Moreover, the photon energy can modulate the total number of groups of the oscillation structures. The unique magneto-optical properties, the beating oscillations and the largest variation in reflectance spectrum, could be confirmed by magneto-optical spectroscopy measurements [35, 36, 49, 50].

Acknowledgments

This work was supported by the NSC and National Center for Theoretical Sciences of Taiwan, under the Grant No. NSC 98-2112-M-006-013-MY4.

References

- [1] K.F. Mak, J. Shan, T.F. Heinz, Phys. Rev. Lett. 104 (2010) 176404.
- [2] A. Grüneis, C. Attaccalite, L. Wirtz, H. Shiozawa, R. Saito, T. Pichler, A. Rubio, Phys. Rev. B 78 (2008) 205425.
- [3] J. Adler, J. Zaffran, A. Silverman, A. Sorkin, O. Cohen, R. Kalish, Comput. Phys. Commun. 182 (2011) 2009.
- [4] S. Yuan, R. Roldán, and M. I. Katsnelson, Phys. Rev. B 84 (2011) 125455.
- [5] M. Koshino, New J. Phys. 15 (2013) 015010.
- [6] Y. Liu, W.S. Lew, S. Goolaup, H.F. Liew, S.K. Wong, T. Zhou, ACS Nano 5 (2011) 5490.
- [7] B. Partoens, F. M. Peeters, Phys. Rev. B 74 (2006) 075404.
- [8] Y. Hao, Y. Wang, L. Wang, Z. Ni, Z. Wang, R. Wang, C.K. Koo, Z. Shen, J.T.L. Thong, Small 6 (2010) 195.
- [9] S. Cheon, K.D. Kihm, J.S. Park, J.S. Lee, B.J. Lee, H. Kim, B.H. Hong, Opt. Lett. 37 (2012) 3765.
- [10] T. Kaplas, A. Zolotukhin, Y. Svirko, Opt. Express 19 (2011) 17226.
- [11] O.L. Berman, G. Gumbs, Y. E. Lozovik, Phys. Rev. B 78 (2008) 085401.
- [12] Z.S. Wu, W. Ren, L. Gao, B. Liu, C. Jiang, H.M. Cheng, Carbon 47 (2009) 493.
- [13] J.-C. Charlier, J.-P. Michenaud, X. Gonze, J.-P. Vigneron, Phys. Rev. B 44 (1991) 13237.
- [14] L. Samuelson, Inder P. Batra, C. Roetti, Solid State Commun. 33 (1980) 817.
- [15] J.-C. Charlier, J.-P. Michenaud, X. Gonze, Phys. Rev. B 46 (1992) 4531.

- [16] D.D.L. Chung, *J. Mater. Sci.* 37 (2002) 1475.
- [17] K. Berland, Ø. Borck, P. Hyldgaard, *Comput. Phys. Commun.* 182 (2011) 1800.
- [18] J.K. Lee, S.C. Lee, J.P. Ahn, S.C. Kim, J.I.B. Wilson, P. John, *J. Chem. Phys.* 129 (2008) 234709.
- [19] R.B. Chen, Y.H. Chiu, *J. Nanosci. Nanotechnol.* 12 (2012) 2557.
- [20] Y.H. Ho, J. Wang, Y.H. Chiu, M.F. Lin, W.P. Su, *Phys. Rev. B* 83 (2011) 121201(R).
- [21] C.H. Ho, C.P. Chang, W.P. Su, M.F. Lin, *New J. Phys.* 15 (2013) 053032.
- [22] J.W. McClure, *Phys. Rev.* 119 (1960) 606.
- [23] Igor A. Luk'yanchuk, Y. Kopelevich, *Phys. Rev. Lett.* 93 (2004) 166402.
- [24] Igor A. Luk'yanchuk, Y. Kopelevich, *Phys. Rev. Lett.* 97 (2006) 256801.
- [25] B.A. Bernevig, T.L. Hughes, S. Raghu, D.P. Arovas, *Phys. Rev. Lett.* 99 (2007) 146804.
- [26] A.N. Ramanayaka, R.G. Mani, *Phys. Rev. B* 82 (2010) 165327.
- [27] Y. Zheng, T. Ando, *Phys. Rev. B* 65 (2002) 245420.
- [28] R.B. Chen, Y.H. Chiu, M.F. Lin, *Carbon* 54 (2013) 268.
- [29] C.H. Ho, Y.H. Ho, Y.Y. Liao, Y.H. Chiu, C.P. Chang, M.F. Lin, *J. Phys. Soc. Jpn.* 81 (2012) 024701.
- [30] K.-C. Chuang, A.M.R. Baker, R.J. Nicholas, *Phys. Rev. B* 80 (2009) 161410(R).
- [31] Y.H. Ho, Y.H. Chiu, W.P. Su, M.F. Lin, *Appl. Phys. Lett.* 99 (2011) 011914.
- [32] T. Matsui, H. Kambara, Y. Niimi, K. Tagami, M. Tsukada, H. Fukuyama, *Phys. Rev. Lett.* 94 (2005) 226403.

- [33] J.M. Schneider, M. Orlita, M. Potemski, D.K. Maude, Phys. Rev. Lett. 102 (2009) 166403.
- [34] M. Orlita, C. Faugeras, J.M. Schneider, G. Martinez, D.K. Maude, M. Potemski, Phys. Rev. Lett. 102 (2009) 166401.
- [35] Z.Q. Li, S.-W. Tsai, W.J. Padilla, S.V. Dordevic, K.S. Burch, Y.J. Wang, D.N. Basov, Phys. Rev. B 74 (2006) 195404.
- [36] L.-C. Tung, P. Cadden-Zimansky, J. Qi, Z. Jiang, D. Smirnov, Phys. Rev. B 84 (2011) 153405.
- [37] Y.H. Lai, J.H. Ho, C.P. Chang, M.F. Lin, Phys. Rev. B, 77 (2008) 085426.
- [38] C.P. Chang, C.L. Lu, F.L. Shyu, R.B. Chen, Y.K. Fang, M.F. Lin, Carbon, 42 (2004) 2975.
- [39] L.G. Johnson, G. Dresselhaus, Phys. Rev. B 7 (1973) 2275.
- [40] E.A. Taft, H.R. Philipp, Phys. Rev. 138 (1965) A197.
- [41] C.W. Chiu, S.H. Lee, S.C. Chen, F.L. Shyu, M.F. Lin, New J. Phys. 12 (2010) 083060.
- [42] M. Koshino, T. Ando, Phys. Rev. B 77 (2008) 115313.
- [43] M.L. Sadowski, G. Martinez, M. Potemski, C. Berger, W.A. de Heer, Phys. Rev. Lett. 97 (2006) 266405.
- [44] C.F. Chen, C.H. Park, B.W. Boudouris, J. Horng, B. Geng, C. Girit, A. Zettl, M.F. Crommie, R.A. Segalman, S.G. Louie, F. Wang, Nature 471 (2011) 617.
- [45] S.M. Collins, P. A. Midgley, Phys. Rev. B 87 (2013) 235432.
- [46] M.F. Lin, F.L. Shyu, J. Phys. Soc. Jpn. 69 (2000) 607.
- [47] W.W. Toy, M.S. Dresselhaus, G. Dresselhaus, Phys. Rev. B 15 (1977) 4077.
- [48] W.J. Padilla, Z.Q. Li, K.S. Burch, Y.S. Lee, K.J. Mikolaitis, D.N. Basov, Rev. Sci. Instrum. 75 (2004) 4710.

- [49] E.A. Henriksen, P. Cadden-Zimansky, Z. Jiang, Z.Q. Li, L.-C. Tung, M.E. Schwartz, M. Takita, Y.-J. Wang, P. Kim, H.L. Stormer, Phys. Rev. Lett. 104 (2010) 067404.
- [50] I. Crassee, J. Levallois, A.L. Walter, M. Ostler, A. Bostwick, E. Rotenberg, T. Seyller, D. van der Marel, A.B. Kuzmenko, Nature Phys. 7 (2011) 48.

FIGURE CAPTIONS

Fig. 1. The vertical optical excitations at $B_0 = 20$ T due to the Landau subbands for (a) the intraband and (b)-(d) interband excitations. The allowed excitations are confined by two arrows of the same color. The square brackets and the parentheses represent the intraband and interband excitations, respectively.

Fig. 2. The joint density of states corresponding to the Fig. 1 for the (a) intraband (b) interband optical excitations.

Fig. 3. (a) The optical absorption spectrum, (b) the real part, and (c) the imaginary part of the dielectric function are shown for field strengths 20 T, 10 T and zero.

Fig. 4. (a) The loss function with respect to three different field strengths. (b) Plasmon frequencies versus field strengths. Each curve corresponds to a specific interband excitation.

Fig. 5. (a) The magnetorefectance spectrum and (b) the relative magnetorefectance spectrum for different field strengths.

Fig. 6. The relative magnetorefectance with respect to the field strength reveals distinct groups of oscillation structures. Panels (a)-(c) represent different photon energies.